Finite element modelling of surface acoustic wave device based corrugated microdiaphragms

Don W Dissanayake[1,2]**, Said Al-Sarawi**[1,2]**, Tien-Fu Lu**[3] **and Derek Abbott**[1,2,4]

[1] Centre for High Performance Integrated Technologies and Systems (CHiPTec), University of Adelaide, SA 5005, Australia
[2] School of Electrical and Electronic Engineering, University of Adelaide, SA 5005, Australia
[3] School of Mechanical Engineering, University of Adelaide, SA 5005, Australia
[4] Centre of Biomedical Engineering (CBME), University of Adelaide, SA 5005, Australia

E-mail: don@eleceng.adelaide.edu.au

Abstract

This paper presents modelling and analysis of microdiaphragms that are designed for implantable micropump applications. Microdiaphragms are considered to be a major component of micropumps. A securely operated, electrostatically actuated, fully passive micropump is designed using a novel method, which is based on surface acoustic wave (SAW) devices and wireless transcutaneous radio frequency (RF) communication. The device is capable of extracting the required power from the RF signal itself, like RFID (ID: identification device) tags; hence the need of a battery and active electronics is negated. Moreover, a SAW correlator is used for secure interrogation of the device. As a result, the device responds only to a unique RF signal, which has the same code as was implanted in the SAW correlator. Finite element analysis (FEA) based on code from ANSYS Inc. is carried out to model the microdiaphragm, and a Rayleigh–Ritz method based analytical model is developed to investigate the validity of the FEA results. During the FEA, a three-dimensional model of the diaphragm is developed and various kinds of corrugation profiles are considered for enhancing the device performance. A coupled-field analysis is carried out to model the electrostatics–solid interaction between the corrugated microdiaphragm and the SAW device. In modelling microdiaphragms, selection of appropriate material properties and element types, application of accurate constraints, and selection of suitable mesh parameters are carefully considered.

(Some figures in this article are in colour only in the electronic version)

1. Introduction

Microelectromechanical system (MEMS) technology is increasingly being applied to develop drug delivery and related microdevices to facilitate various dosing methods. MEMS based drug delivery devices in general include microneedles, osmosis devices, micropumps and biodegradable MEMS devices [1]. However, the miniaturization of macroscale technology has been an inherent restriction on the development of MEMS. Hence, micropumps, that are considered to be an essential component in drug delivery systems, represent a significant challenge in the design of low powered actuation mechanisms.

On the basis of the working principle of micropumps, they can be classified into a host of categories such as electromagnetic, electrostatic, piezoelectric, shape memory and bimetallic [2, 3]. Electrostatic micropumps have attracted attention in recent years since electrostatic actuators can easily be miniaturized and the electrostatic force between two capacitor plates depends on only a few parameters such as the applied voltage, the dielectric media, the distance between the plates, and the effective plate area [3]. For such micropumps
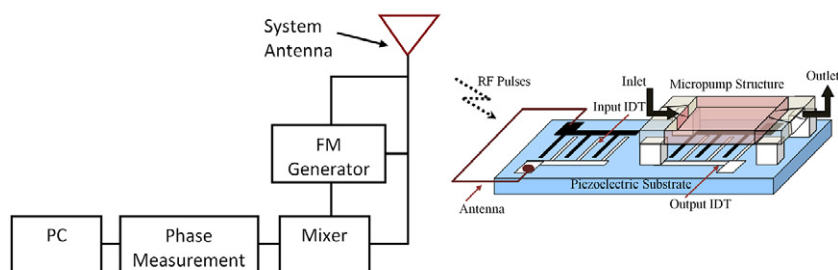
Figure 1. Wireless interrogation unit for the SAW device based micropump. The SAW device consists of a piezoelectric substrate, input IDT, and output IDT. The input IDT is connected to a microantenna for wireless communication. The micropump structure is placed on top of the output IDT of a coded SAW device (the SAW correlator; see section 2.2), which securely controls the microdiaphragm.

that are targeted for use in *in vivo* applications, wireless, secure and batteryless operation is highly desired. Additionally, valveless micropumps are considered very attractive as they are low cost devices because of their simple structure [4].

In the development of micropumps, it is becoming an increasing trend to predict the performance of the micropump before the prototype is fabricated. Various approaches have been pursued in the process of design, development and realization of these micropumps and microfluidic devices. Simulation of diaphragm based, valveless micropumps with the use of FEA tools has become more popular, because of the availability of advanced simulation tools and computational power [1, 5, 6]. Alternatively, analytical models have also been used for the analysis of actuation mechanisms [7–9]. Both of these methods facilitate the design of a model with optimal operating conditions prior to device fabrication.

The optimization and verification of individual components of a micropump to achieve the desired performance of an integrated system is highly important. Therefore, in this paper, the design and analysis of low powered, electrostatically controlled corrugated microdiaphragms is carried out using both FEA and analytical modelling techniques.

The authors present a novel, fully passive, wireless and secure interrogation methodology and an actuation mechanism for operating a micropump for drug delivery and related biomedical applications. Section 2 explains the operation of the micropump structure, and the secure actuation mechanism that is based on SAW device technology. Section 3 is focused on the design of microdiaphragm structures, and in section 4 a Rayleigh–Ritz method based analytical model is discussed. Then in section 5, more emphasis is given to FEM using ANSYS simulation tools [10]. The results achieved through FEA are presented and discussed in section 6. Section 7 highlights challenges and expected future work and is followed by the conclusion.

2. SAW device based wireless electrostatic actuation

2.1. SAW devices

Surface acoustic wave (SAW) devices are widely used in MEMS applications, which require secure, wireless, and passive interrogation [11]. These devices are recognized for

their versatility and efficiency in controlling and processing electrical signals. They are based on the propagation of acoustic waves in elastic solids and the coupling of these waves to electric charge signals via input and output inter-digital transducers (IDT) deposited on a piezoelectric material. As shown in figure 1, a SAW device consists of a solid substrate with input and output IDTs [11]. Since these devices are mostly used for wireless applications, a microantenna has to be attached to the input IDT.

Inclusion of a battery with the implantable device, the requirement of active electronics to incorporate the security features, and hence the need of high operating power are considered to be some of the limitations of currently available implantable microfluidic devices [2, 4, 11]. Moreover, battery powered implants inherit added disadvantages such as the additional mass and the size of the device, and the need to replace the battery, perhaps more than once.

However, the ability to store energy in the SAW, and the possibility of handling high frequencies enables the construction of passive, low cost devices for wireless communication with the capability of being interrogated by RF signals [12]. Moreover, as is elaborated in section 2.2, by using a SAW correlator instead of a standard SAW device, a security feature can be incorporated in the wireless interrogation, with no active electronics being added to the device. As explained in section 2.3, the power required to operate the device is obtained from the interrogating RF signal. Therefore, the device is batteryless and becomes more feasible for implantation use because of its small size and mass. Considering all these factors, this SAW device based novel actuation mechanism is adopted and developed in this research.

2.2. Secure and wireless interrogation

In implantable drug delivery applications, it is important that the device is not triggered by spurious RF signals. A SAW correlator cab is used for wireless, secure interrogation of the device. As depicted in figure 2, the SAW correlator consists of a coded IDT to ensure that the device responds only to a matched RF signal [11].

The acoustic wave propagation can be facilitated by designing the IDT fingers in such a way that their polarity and orientation are related to the input code in the receiving
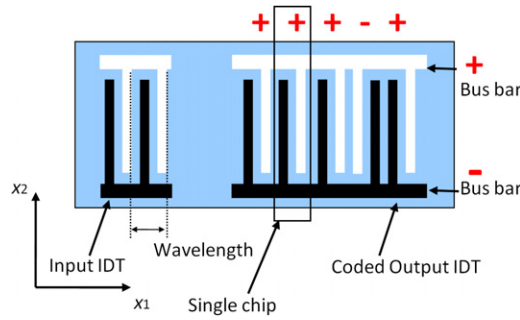
Figure 2. Basic structure of a SAW correlator. The output IDT geometry determines the code of the generated acoustic wave. A five-bit Barker sequence $(+ + + - +)$ is encoded into the output IDT. Referring to the highlighted finger pair: the charge on the first finger creates a negative acoustic pulse and the charge on the second finger creates a positive pulse, hence creating an overall positive pulse. The fourth finger pair is connected to the busbar with opposite sign to the highlighted pair, which generates an overall negative pulse. By ordering the fingers in certain ways it is possible to control the creation of acoustic pulses. This effect is exploited in coding the devices for secure actuation.

Figure 3. Side view: an air-gap separated diaphragm is placed above the output IDT of the SAW device. Top view: the area of the diaphragm is larger than the effective area of the output IDT, and hence allows more deflection as the stress level at the central area of the diaphragm is less.

RF signal. As a result, the code used in the interrogating RF signal needs to be equivalent to the finger pair configuration embedded in the correlator. When a matched code is fed to the correlator, an acoustic wave with the same sign and phase is generated and interacts constructively to generate a signal with a high processing gain. However, if an incorrect code is input to the system, the generated pulses will interact destructively [11]. Therefore, by using a longer code (and hence increasing the number of finger pairs) it is possible to increase the number of unique combinations of control signals. Overall, this enhances the security feature of the device by making it harder to manipulate or abuse the code.

2.3. The micropump operating principle

As can be seen from figure 1, the interrogation approach followed by the authors is based on conventional radio frequency identification device (RFID) technology where low power circuits can obtain their power from an electromagnetic field. Additionally, the implantable device is designed to achieve this by not having any active electronic circuitry. Figure 1 shows a set-up for interrogating a SAW device with an integrated antenna. The valveless micropump structure is mounted on top of the output IDT of the SAW device (the SAW correlator). This micropump structure consists of a thin conductive microdiaphragm, a fluid chamber, and inlet and outlet diffusers. As further elaborated in figure 3, the gap between the conductive diaphragm and the output IDT is set to be a few micrometres.

Here, the SAW device receives a coded RF signal power, which is directly converted to stress waves in the piezoelectric substrate, using the converse piezoelectric effect. These mechanical stress waves propagate along the planar surface of the piezoelectric substrate and are then reconverted to an electric signal at the output IDT because of the piezoelectric effect. However, as explained in section 2.2, only when a
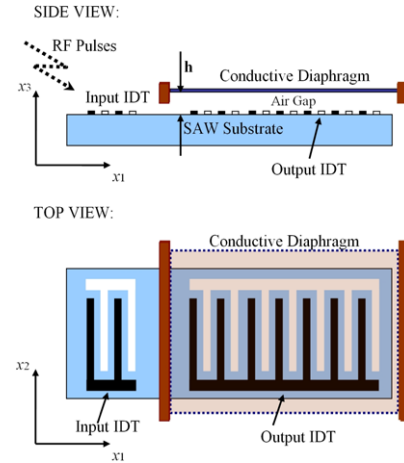
matched RF signal is received is a signal with high amplitude generated at the output IDT. Consequently, an electrostatic field is generated between the output IDT and the conductive diaphragm, and the resulting electrostatic force causes a deflection in the microdiaphragm. This deflection in the microdiaphragm, along with carefully designed diffusers, is used to cause the required microfluidic flow manipulations.

3. Corrugated microdiaphragm modelling

A diaphragm is essentially a thin circular or rectangular plate, made out of a flexible material, stretched and fastened at its periphery. Diaphragms are widely used as sensing elements in MEMS devices, for high accuracy and good dynamic response [13, 14]. A periphery-clamped flat diaphragm having high residual stress in the film may give rise to undesirable effects such as much higher actuation voltage, film buckling, or even membrane cracking. One approach for addressing the stress issue is the utilization of a corrugation technique, which is considered to be an effective way to alleviate the residual stress in the diaphragm [15]. The corrugated diaphragm has been verified to be capable of releasing the built-in stress, thereby increasing the mechanical sensitivity of the diaphragm and reducing the irreproducibility [16]. This results in the requirement of a low actuation voltage to drive microdiaphragm based structures.

Various kinds of corrugation profiles such as sinusoidal, toroidal, sawtooth, and trapezoidal are being used for MEMS applications [15, 17, 18]. Due to the minimal stress concentration feature, sinusoidal and toroidal profiles are found to be attractive, and performance analyses for such profiles are conducted and presented in section 6.

3.1. Corrugation parameters

Parameters L, H, t_D (corrugation thickness) and N (number of corrugation wavelengths) are considered to be the critical
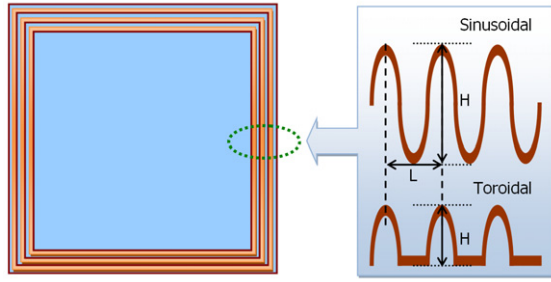
Figure 4. Sinusoidal and toroidal corrugation profiles and corrugation parameters. Here, L denotes the corrugation wavelength and H is the corrugation height.

parameters in the design of sinusoidal and toroidal corrugations as depicted in figure 4. The ratios H/t_D, and L/H need to be carefully considered to reduce the unnecessary stress concentrations around the corrugations [17].

Different methods are mentioned in the literature for the design of the sinusoidal corrugations [17, 18]. Especially in analytical approaches, tangent arcs are often used to develop an approximated sinusoidal shape [7]. Therefore, in order to compare the levels of effectiveness for the various methods, the authors have designed sinusoidal corrugations using two different methods: (i) the approximation of sinusoidal shape with tangent arcs; and (ii) the use of corrugations with purely sinusoidal shape. Then, analysis is conducted to evaluate the performance of diaphragms with these kinds of sinusoidal corrugations, along with the toroidal-shaped corrugations, and results are elaborated in section 6.

4. The analytical model for the microdiaphragm actuation

4.1. Electrostatic force generation

In electrostatic actuation, the electrostatic attraction force F applied on two parallel conductive plates (electrodes) can be described using the parallel plate capacitor effect [4] as

$$F = \frac{1}{2} \frac{\varepsilon A \Phi^2}{(h - W_D)^2}, \tag{1}$$

where ε is the dielectric coefficient of the medium between the plates, A is the effective plate area, W_D is the instantaneous deflection of the microdiaphragm in the x_3 direction, h is the initial plate spacing, and Φ is the applied electric potential, between the plates.

In the authors' previous work [19, 20], the electric potential at the output IDT region was found to be a combination of the electric potential at the IDT fingers and the electric potential at the IDT finger gaps, and this is shown in equation (2).

$$\Phi(x_1, x_3, t) = \begin{cases} \Psi, & \text{for } n \leqslant x_1 \leqslant (\frac{1}{4} + n)\lambda \\ \Omega, & \text{for } (\frac{1}{4} + n)\lambda < x_1 < (\frac{1}{2} + n)\lambda \\ -\Psi, & \text{for } (\frac{1}{2} + n)\lambda \leqslant x_1 \leqslant (\frac{3}{4} + n)\lambda \\ -\Omega, & \text{for } (\frac{3}{4} + n)\lambda < x_1 < (1 + n)\lambda, \end{cases} \tag{2}$$
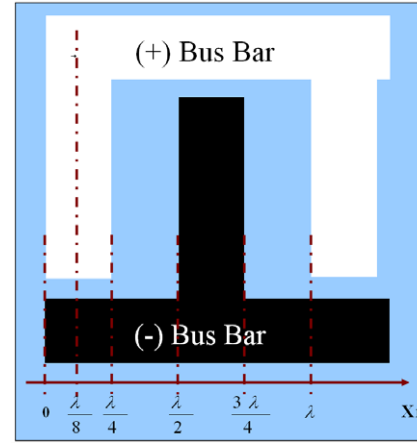
Figure 5. IDT finger representation for one wavelength (λ) with a metallization ratio of $\frac{1}{2}$.

where

$$\Psi = \frac{2T}{\pi^2} \Phi\left(\frac{\lambda}{8}, x_3, t\right), \qquad \Omega = \Phi(x_1, x_3, t)$$

and $n = 0, 1, 2, \ldots, N_p - 1$

for $\Phi(x_1, x_3, t) = \left[\sum_m C_m \alpha_4^m e^{ikb^m x_3}\right] e^{ik(x_1 - vt)}.$

Here N_p is the total number of finger pairs in the output IDT, and λ is the SAW wavelength. The C_m values are the weighting coefficients of these electric potential equations and are defined on the basis of the mechanical and electrical boundary conditions of the system [19]. These α_4^m values are linear coefficients that are dependent on the decay constant b, and $m = 1, 2, 3, 4$. v is the SAW velocity in the piezoelectric substrate in the x_1 direction, k is the wavenumber, and T ($= \lambda/v$) is the time period of the SAW. The coordinate system used in these equations is defined in figure 3 and the IDT geometry for one wavelength (one period) of the SAW is shown in figure 5.

As is explained in section 2.3, an electrostatic force is generated between the output IDT and the conductive diaphragm, because of the time varying electric potential at the output IDT. To formulate this force, each finger gap is divided into N_s subdivisions in the x_1 direction, so that each subdivision has a width of $\frac{f_w}{N_s}$ and a length of f_l ($\approx$aperture of the IDT). Combining equations (1) and (2), and after some algebraic simplifications, the total resultant electrostatic force can be evaluated as

$$\mathbf{F}_{(Tot)} = \frac{C}{(h - W_D)^2}$$

$$\times \sum_j \left[\left(\frac{2T}{\pi^2}\right)^2 \Phi^2\left(\frac{\lambda}{8}, x_3, t\right) + \Phi^2\left(\frac{\lambda}{4} + \frac{j\lambda}{4N_s}, x_3, t\right) \right], \tag{3}$$

for $j = 1, 2, 3, \ldots, N_s$ and $C = \frac{\varepsilon_0 f_l f_w N_p}{N_s}$. While the diaphragm is stretched because of the applied electrostatic force, an elastic restoring force is developed in the diaphragm. At equilibrium, the diaphragm's kinetic energy becomes zero. Therefore, to determine the displacement achieved by the

diaphragm, the calculated electrostatic force and the elastic restoring force need to be considered at their equilibrium point [21, 22]. However, this becomes a complex problem to solve as both forces depend on the instantaneous diaphragm displacement W_D. Therefore, to obtain an accurate solution for W_D, analytical methods or numerical analysis methods such as FEA have to be used. Both of these methods are exploited in this research to analyse the corrugated diaphragm performance. The analytical model discussed here is used to validate the results obtained from FEA simulations.

4.2. The Rayleigh–Ritz method

This analysis is an extended version of the authors' previous work [20], which was developed to analyse the performance of a SAW device based electrostatic actuator using the Rayleigh–Ritz method. Here, an energy minimization technique is used to solve the problem for the corrugated diaphragm model.

For a rectangular microdiaphragm with a length of $2a$ and a width of $2b$, the total energy $E_{(Tot)}$ of the diaphragm under pressure P can be written as [23]

$$\mathbf{E}_{(Tot)} = E1 - E2 - E3,$$

$$E1 = \int_{-b}^{b} \int_{-a}^{a} \frac{D}{2} \left(\frac{\partial^2 W_D}{\partial x_1^2} + \frac{\partial^2 W_D}{\partial x_2^2} \right)^2 dx_1 \, dx_2$$

$$E2 = \int_{-b}^{b} \int_{-a}^{a} D(1-\nu) \left[\frac{\partial^2 W_D}{\partial x_1^2} \frac{\partial^2 W_D}{\partial x_2^2} - \left(\frac{\partial^2 W_D}{\partial x_1 \partial x_2} \right)^2 \right] dx_1 \, dx_2$$

$$E3 = \int_{-b}^{b} \int_{-a}^{a} P W_D \, dx_1 \, dx_2$$

(4)

where $D = \frac{E t_D^3}{12(1-\nu^2)}$ is the bending stiffness, E is the modulus of elasticity, t_D is the diaphragm thickness and ν is the Poisson ratio of the diaphragm material. Considering the relation $F = P A_{eff}$, where A_{eff} is the effective diaphragm area, the term $E3$ in equation (4) can be rearranged using the electrostatic force derived in equation (3).

Now, on the basis of the essential boundary conditions of the model (i.e., the displacements and their first derivatives on the boundary), a displacement function for the rectangular diaphragm is considered as in equation (5), with the only unknown being the constant K.

$$W_D(x_1, x_2) = K(a^2 - x_1^2)^2 (b^2 - x_2^2)^2. \quad (5)$$

Here, $(x_1, x_2) \equiv (0, 0)$ denotes the centre of the diaphragm in the $x_1 x_2$ plane. Constant K can be evaluated by substituting equations (3) and (5) into equation (4), and by minimizing the total oenergy $\mathbf{E}_{(Tot)}$ with respect to K. An iterative approach is needed, to achieve the convergence, because of the complicated nonlinear coupling of equations (3)–(5).

In order to utilize this analytical model to analyse the performance of the corrugated microdiaphragm and hence to validate FEA simulations, the equivalent bending stiffness method [7] and residual stress reduction method [15, 24] are used for sinusoidal and toroidal profiles respectively. However, to reduce the complexity of the model, these methods are

associated with some assumptions and simplifications such as ignoring the bending stiffness in the tangential direction for highly stressed and shadow corrugations, and ignoring the Poisson effect for the corrugated part as corrugations are deformed much more easily.

In general, analytical approaches with less simplification are quite complicated and require extensive computational effort. It is known that more accurate results for such problems can be achieved through numerical analysis using mathematical methods such as finite element analysis (FEA) [23, 25]. Because of the complexity in analysis, which involves electrostatic and structural field couplings in a complicated geometry, FEA of the corrugated microdiaphragm is developed using ANSYS simulation tools and presented in section 5.

5. ANSYS based finite element modelling

For finite element analysis (FEA) of the device, a coupled-field analysis is required to model the electrostatics–solid interaction. A load transfer method based ANSYS multi-field solver (MFX) is available for a large class of coupled analysis problems, and is more suitable for MEMS based coupled-field analysis which involves interaction between multiple physical fields [1, 10]. Therefore, an ANSYS-MFX solver is considered to be highly suitable for the analysis of the novel micropump actuation mechanism, and is used to carry out the analysis of the microdiaphragm performance.

### 5.1. Preparation of the model for the analysis

The accuracy of FEA depends on factors such as the node density of the mesh, appropriate element type, and accurate application of boundary conditions. Additionally, these factors lead to a tradeoff between accuracy and simulation time. Therefore, extra care is needed in meshing the geometry, especially during the analysis of the effect of the corrugation parameters.

Here, the SOLID95 element type is used for the structural model including 3D corrugations, since it can tolerate irregular shapes without as much loss of accuracy compared to the other SOLID elements in ANSYS [10]. Additionally, SOLID95 elements are well suited for modelling curved boundaries, and have capabilities such as plasticity, creep, stress stiffening, large deflection, and large strain capability, hence being highly suitable for the design of corrugations [26]. The electrostatic air-gap beneath the diaphragm is meshed using the SOLID122 element type. SOLID122 elements have compatible voltage shapes and are applicable in 3D electrostatic and time-harmonic electric field analysis [10].

5.2. Effective mesh generation

In electrostatics–solid coupling, forces get transferred from the electrostatic field to the solid diaphragm and displacements get transferred from the solid to the electrostatic field, which requires a suitable mesh density at the interface.

In this model, the effect of the output IDT is incorporated by coupling a set of nodes at the bottom of the air-gap to
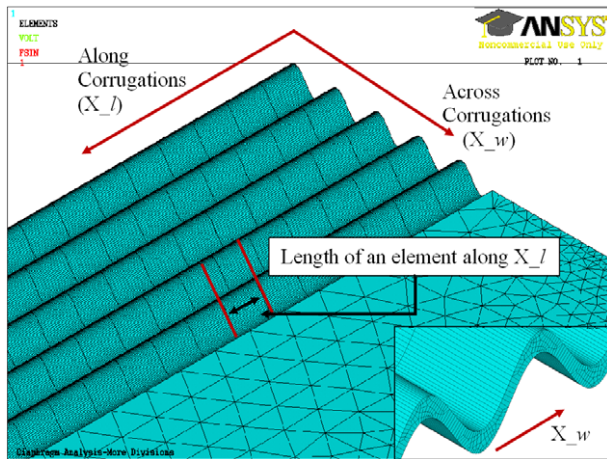
Figure 6. View of the corrugations in the meshed diaphragm model. X_l denotes the direction along the corrugations and X_w denotes the direction across the corrugations towards the mid-section.

match the desired IDT pattern and assigning the VOLT degree of freedom (DoF) to those nodes. It should be noted that the width of each IDT finger (and finger gaps) is designed to be 10 μm ($=\lambda/4$ for an operating SAW frequency of 50 MHz and a SAW velocity of 4000 m s^{-1}). Therefore, for an accurate representation of the output IDT, smaller element size is needed in the air-gap model as well. In total, approximately 300 000–350 000 nodes are used for these simulations to achieve the expected accuracy. With the availability of systems with high processing power, such simulations have become more practicable than in the past.

During the initial analysis, simulations were carried out with differently meshed models until the results converged. This is to highlight the fact that accurate results depend not only on the node density, but also on how well the critical sections are meshed, considering the physics associated with the model. Figure 6 explains the different directions considered in each approach, for varying the node density in corrugated and flat sections.

In a first approach, the node density is changed along the X_l direction by varying the length of the elements. However, this in turn causes an effect on the node density of the flat section of the diaphragm as can be seen from figure 7. In a second approach, the node density is varied along the X_w direction. Once the resolution in the corrugated section is established, the element size in the flat section is varied to allow deciding upon an appropriate mesh for the flat section, to represent the output IDT accurately. The way in which these changes affect the accuracy is further discussed in section 5.3.

5.3. The effect of the mesh density on the accuracy

Three kinds of mesh variations are considered in initial simulations and the convergence results are presented in figure 8. Here, the percentage variation is the variation in the mid-node displacement of the diaphragm from one simulation to the next simulation, as the total number of nodes is increased.

Table 1. Material properties used for the corrugated diaphragm design [27–30].

Material property	PI-2610	Si$_3$N$_4$	Al
Density (kg m^{-3})	1400	3184	2770
Poisson's ratio	0.22	0.24	0.33
Elastic modulus (GPa)	7.5	169	71

In general, results converge (the percentage variation decreases to 1%) as the total number of nodes used for the model increases. However, there is not much variation in results as the node density is changed along X_l. This is because the bending stiffness in the corrugations along the X_l direction is negligible and hence does not contribute much to the sensitivity [24], and addition of extra nodes along that direction makes little difference.

In contrast, higher variations are observed when the node density is changed along the X_w direction. It is known that the tensile rigidity in the radial direction is smaller in a corrugated diaphragm and has a dominant effect on the overall sensitivity [17]. Additionally, when the diaphragm is deflected because of the applied electrostatic force, an elastic restoring force is generated in the diaphragm that is directed towards the diaphragm centre. As a result, a higher node density in the X_w direction allows a better representation of the corrugations and produces more accurate results.

Similarly, smaller element sizes in the flat section (including the air-gap) have a substantial effect on the overall accuracy. Smaller elements in the flat section allow a good representation of the output IDT structure and also increase the accuracy of the interpolations at the fluid–structure interface during simulations. Therefore as the element size decreases from 15 to 3 μm over a few simulations, convergence is noticed. However, an element size of 5 μm is selected for the rest of the simulations as it produces results within only 1% variation.

5.4. Material selection

As was mentioned before, the micropump device is targeted at biomedical applications. Therefore a careful selection of bio-compatible materials is highly important. The mechanical properties of the chosen materials are shown in table 1. The corrugated microdiaphragm consists of three main sections with different materials: the flat section, the corrugated section and the conductive thin metal section, as can be seen in figure 9.

(i) Flat section: silicon nitride (Si$_3$N$_4$) is chosen for the flat part of the diaphragm, because of its high strength over a wide temperature range, outstanding wear resistance, and good electrical insulation; hence the fluid in the pumping chamber is isolated from the electrostatic field.

(ii) Corrugated section: polymer based bio-MEMS has become more and more popular, mainly because it has a very low stiffness and inherently provides adequate flexibility (reduced micromotion strain) for most of the low powered operations [4, 31]. Here, polyimide PI-2610 is chosen for the corrugated section of the diaphragm. The rigid rod polyimide structure of cured PI-2600 products
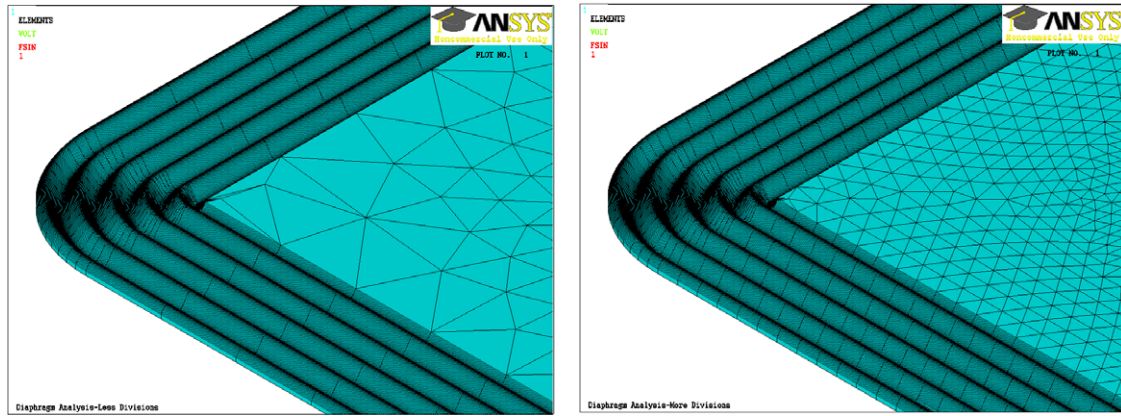
Figure 7. Meshed corrugations with 25 divisions (left) and 75 divisions (right) per side along *X_l*. They result in a coarse and a finer mesh respectively. The mesh density in the corrugated section affects the mesh density in the adjacent flat section.
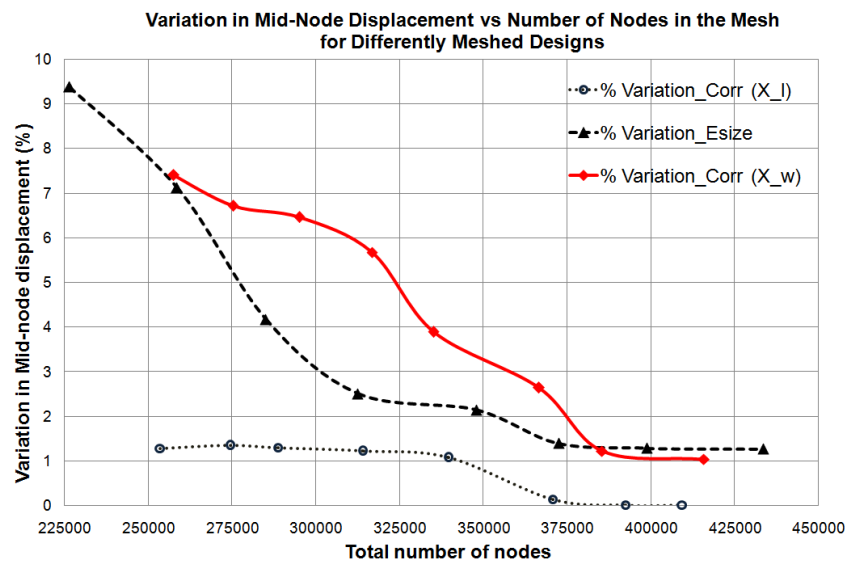
Figure 8. The percentage variation in mid-node displacement (PVMD) of the diaphragm versus the total number of nodes. Three scenarios are considered. % Variation_Corr (*X_l*): the PVMD as the node density is varied along the *X_l* direction. % Variation_Esize: the PVMD as the element size is varied for the flat section. % Variation_Corr (*X_w*): the PVMD as the node density is varied along the *X_w* direction. *X_l* and *X_w* are defined in figure 6.

exhibits a desirable combination of film properties such as low stress, low coefficient of thermal expansion (CTE), high elastic modulus compared with other polyimides, and good ductility for microelectronic applications [27]. These attractive features help to generate low stress and high displacement in the diaphragm, and more importantly, facilitate comparatively easy and consistent fabrication of the corrugations around the flat section of the diaphragm.

(iii) Conductive metal section: aluminium (Al) is chosen as the material for defining metal connections in the micropump device. This is mainly because of the comparatively low elastic modulus and Poisson's ratio, and low cost. However, gold (Ag) could be used as a better alternative to Al, considering the good conductivity, high bio-compatibility, and the possibility of clean and neat deposition of thin layers on the nanometre scale.

5.5. Boundary conditions

Once the geometry is meshed, the model needs then to be constrained by applying appropriate boundary conditions. There are two kinds of boundary conditions related to this model: (i) structural (mechanical constraint) and (ii) electrical (electrostatic constraint) boundary conditions.

(i) Structural boundary conditions: the microdiaphragm is fully clamped to the micropump chamber and represented by constraining all the displacements of nodes associated with the wall. Since the quarter symmetry is implemented in the design to save design and simulation time, the structural symmetry condition is applied at the inner areas of the diaphragm and the air-gap as shown in figure 9.

(ii) Electrical boundary conditions: to mimic the effect of the thin conductive (aluminium) coating at the bottom surface of the diaphragm, all the nodes on the bottom surface are
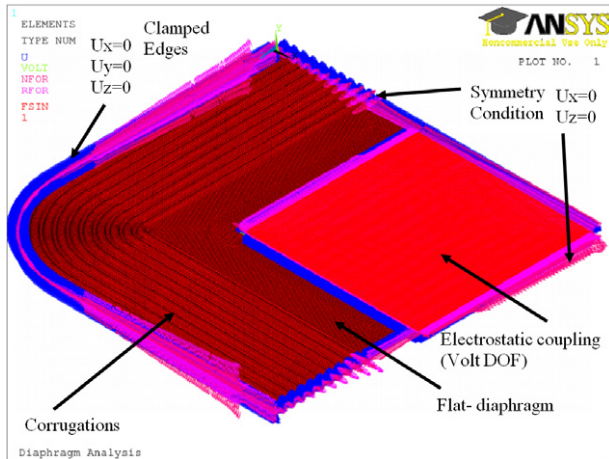
Figure 9. Boundary conditions applied in the design to reflect the expected constraint. The quarter symmetry is exploited to reduce the simulation time and CPU usage. The dimensions of the quarter-diaphragm segment are 1000 μm $\times$ 5 μm $\times$ 1000 μm (length/2 $\times$ height $\times$ width/2). The height of the air-gap is 5 μm.

Figure 10. Contour plot of the displaced diaphragm structure with sinusoidal corrugations. Displacement is a maximum at the middle part of the diaphragm.

coupled and a Volt DoF is applied. Additionally, to mimic the effect of the output IDT, two different sets of nodes are carefully selected at the bottom surface of the air-gap for each IDT electrode (positive and negative electrodes). As this approach negates the need of extra volumes for the thin metal coating and the output IDT electrodes, the FEA becomes easier and more time efficient.

6. Simulation and result analysis

Results obtained from the ANSYS based FEA of corrugated microdiaphragm actuation are presented and analysed in this section. Additionally, analytical model based preliminary results are used to validate the FEA simulations.

6.1. Displacement results for different kinds of corrugations

As was discussed in section 3, two kinds of sinusoidal and toroidal corrugations were designed and analysed. In this analysis, corrugation parameters (L, H, t_D and N), element types, material properties and all of the other design parameters and constraints were kept unchanged except the corrugation type. Therefore the mid-diaphragm displacements reflect the effectiveness of each corrugation type in the SAW device based microdiaphragm actuation. Figure 10 depicts a contour plot of the simulated diaphragm structure with sinusoidal corrugations.

Deformation results achieved from FEA and the analytical model for various corrugation types are presented in figure 11. As expected, quadratic-shaped curves are observed, in line with the theoretical relationship between the applied electric potential and the displacement. More importantly, these corrugated diaphragms have achieved higher microdisplacements for low operating voltages compared to ones in published research [19, 32], and the displacement
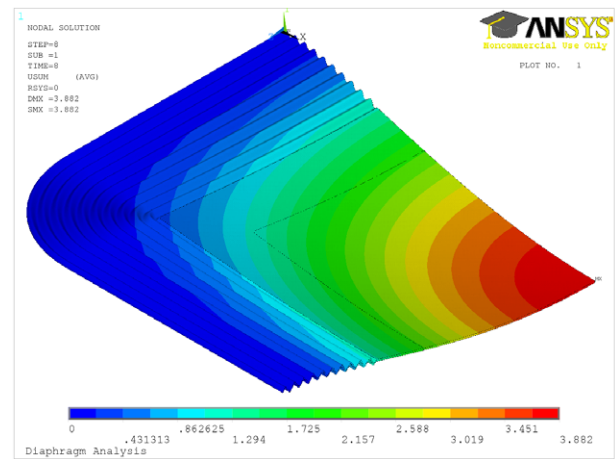
achieved by any kind of corrugated diaphragm is higher than that of a flat diaphragm.

It can be noted that analytical and FEA results show a good correlation in general. The apparent slight deviation in analytical results compared to FEA results is believed to arise because of the simplifications made to the model during the analytical analysis. For instance, the fringing capacitor effect, between the electrodes and IDT fingers, reduces the energy available for the actuation and this can cause a slight reduction in deflection achieved in the FEA model. However, such effects are not included in the analytical model and hence slightly higher deflections are observed.

Now that we have developed confidence in the FEA modelling, the rest of the analysis is carried out on the basis of corrugations of purely sinusoidal type, since these show better deformations than ones of other types.

### 6.2. The effect of the corrugation wavelength

Deflections achieved using a diaphragm with purely sinusoidal corrugations are analysed for different corrugation wavelengths (L) while keeping other corrugation parameters unchanged ($H = 20$ μm, $t_D = 5$ μm and $N = 5$). FEA is carried out for different actuation voltages and results are presented in figure 12.

Higher displacements can be observed around $L = 15$ μm, and the deflections tend to decrease as the corrugation wavelength increases. This is because for within the selected ratio H/t_D, larger corrugation lengths increase the effective thickness of the diaphragm; hence the flexural rigidity increases, and the mechanical sensitivity reduces as a result [15]. Wavelengths less than 10 μm can be discarded, since practically it is difficult to fabricate narrower corrugations.
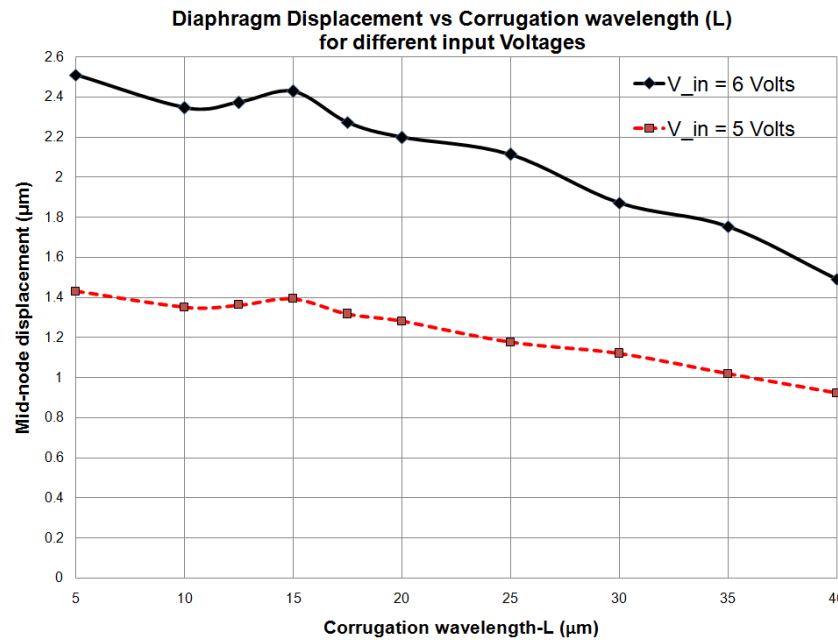
6.3. Stress distribution around the corrugations

Stress analysis is also carried out using ANSYS methods to analyse the ability of the microdiaphragm to withstand the

Diaphragm Displacement vs Applied Voltage for different corrugation types
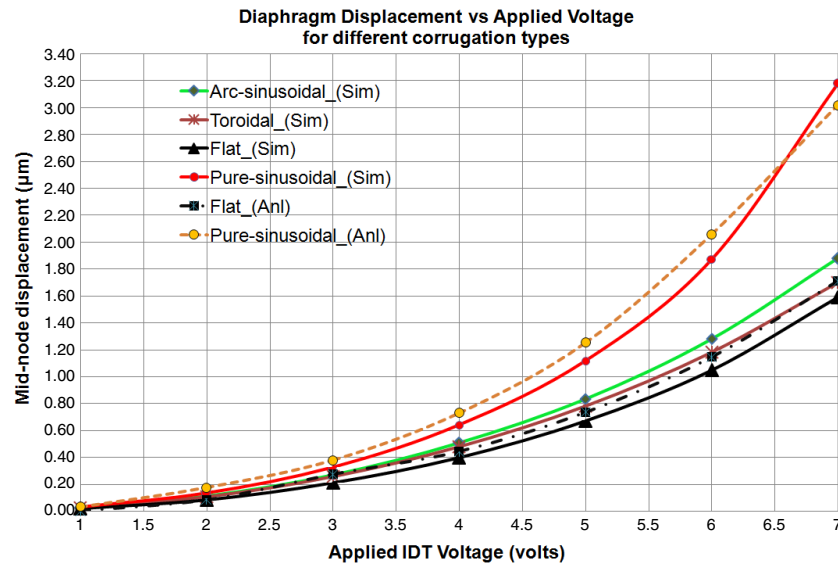
Figure 11. Comparison of diaphragm displacements of different kinds of corrugations: purely sinusoidal, toroidal, approximated sinusoidal with tangent arcs, and flat diaphragm. Note that the corrugation parameters are $L = 30 \ \mu$m, $H = 20 \ \mu$m, $t_{\mathrm{D}} = 5 \ \mu$m and $N = 5$.

Diaphragm Displacement vs Corrugation wavelength (L) for different input Voltages

Figure 12. The variation in displacement for different L, for input IDT voltages of 5 and 6 V, and $H = 20 \ \mu$m, $t_{\mathrm{D}} = 5 \ \mu$m and $N = 5$.

applied mechanical forces. Contour plots of the von Mises stress distribution around corrugations of the diaphragm for $N = 5$ and 10 are shown in figure 13. Here, von Mises stress can be used to predict the yielding of any of the three materials used, under any loading condition. In either of these scenarios, the maximum von Mises stress is less than 0.5 MPa, which is much lower that the yield strengths of the selected materials. This demonstrates that the diaphragm's deflection is well within the elastic range of the materials used. Additionally in both the scenarios, much of the stress is concentrated into the first few corrugations, and the maximum von Mises stress values do not differ by much. Therefore, on the basis of the simulations it is evident that having extra corrugations does not

greatly improve the stress distribution obtained, but increases the fabrication difficulty by requiring us to fabricate more corrugations.

7. Discussion and future work

7.1. Issues in microfluidic interaction

Highly sensitive capacitive diaphragms would be suitable for sensing applications, but could cause problems in actuating applications. However, it has been shown that comparatively stiff materials in the flat section increase the overall stability of the diaphragm in similar applications [33]. Therefore the design presented is considered to be effective and viable.

9
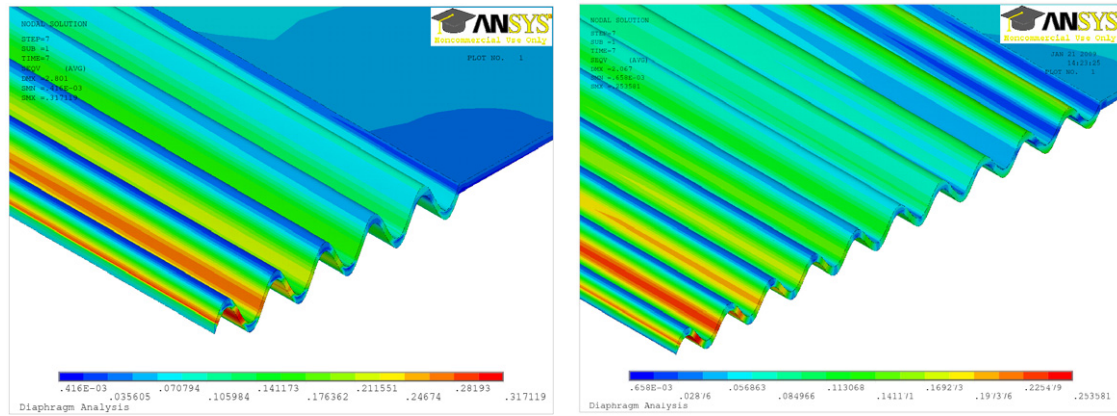
Figure 13. Von Mises stress distribution around corrugations for a purely sinusoidal corrugated design. Left: number of corrugations $N = 5$. Right: $N = 10$, for $H = 20$ μm, $t_D = 5$ μm and $L = 20$ μm.

The back pressure issue also has to be considered, as it is known to affect the flow rate in valveless diffuser micropumps. This can be minimized by incorporating curved inlets in diffusers, and carefully selecting diffuser parameters such as the diffuser angle and length for a laminar flow condition with low Reynolds numbers (<400) [8, 34]. Following such approaches, a maximum ratio of 2.23 between forward and backward flow has been calculated for this type of diffuser, which is sufficient for a pumping effect [35].

In micropumps, the resonance frequency of the microdiaphragm is damped by the fluidic environment around it, and various approaches have been investigated and presented in the literature with successfully realized devices [8, 25, 33, 35]. But in SAW device based interrogation, the device actuating frequency can be easily controlled without affecting the SAW frequency and the implanted code. Therefore, an optimal operating condition can be achieved by matching the control signal frequency to the damped resonance frequency of the device, allowing sufficient relaxation and minimum energy loss [11, 35].

7.2. Device integration

The microfluidic device consists of three main components: the micropump, the SAW device and the microantenna. Initial fabrication has started and is expected to continue in four phases. In phase 1, the coded SAW device has already been fabricated and tested as a stand-alone component. As part of phase 2, the microdiaphragm is being fabricated, along with the chamber consisting of valveless diffusers. During phase 3, the integration and testing of the pumping chamber and the SAW device is expected. In the final phase, the fabrication of the antenna and the integration of the whole device are to be performed.

As potential future work, in addition to device fabrication, the multiple-code coupling method in the ANSYS-MFX solver combined with ANSYS-CFX could be used to develop and simulate a complete electrostatics–structure–fluid interaction problem, to optimize the design parameters of the desired micropump. This will allow a complete simulation model that could be used to analyse similar microfluidic devices before fabrication.

8. Conclusion

A novel, wirelessly and securely interrogated, batteryless and passive micropump device is discussed in this paper. The device is designed to be small in size and mass, and with biocompatible materials, to enable it to be used in biomedical applications such as drug delivery, DNA sequencing, and flow cytometry. The importance of coded SAW devices incorporating a secure and wireless interrogation is discussed. Characteristics of the corrugated microdiaphragm design are presented and the electrostatic actuation of such a diaphragm with the use of a SAW device is also presented.

A Rayleigh–Ritz method based analytical model is developed mainly to validate the results obtained through FEA. The significance of the use of FEA to simulate and analyse complex scenarios as an alternative to analytical modelling is highlighted. Moreover, ANSYS-MFX based finite element modelling is carried out to evaluate the performance of corrugated microdiaphragms, and the relationship between different corrugation types, corrugation parameters, material properties, and design practices, for the diaphragm performance, is also presented. It is demonstrated that use of polyimide based sinusoidal corrugations and a square-shaped diaphragm produces more deflections compared to using a flat diaphragm. Moreover, the stress distributions around corrugations are discussed. Expected future work including the overall parameter optimization and modelling of more complicated behaviour of the micropump operation with liquid loading is highlighted.

References

[1] Nisar A, Afzulpurkar N, Mahaisavariya B and Tuantranont A 2008 Multifield analysis using multiple code coupling of a MEMS based micropump with biocompatible membrane materials for biomedical applications *Int. Conf. on Biomedical Engineering Informatics (march)* vol 1, pp 531–5

[2] Nguyen N T, Huang X and Chuan T K 2002 MEMS-micropumps: a review *Trans. ASME J. Fluids Eng.* **124** 384–92

[3] Ng T Y, Jiang T Y, Li H, Lam K Y and Reddy J N 2004 A coupled field study on the non-linear dynamic characteristics of an electrostatic micropump *J. Sound Vib.* **273** 989–1006

[4] Tsai N C and Sue C Y 2007 Review of MEMS-based drug delivery and dosing systems *Sensors Actuators* A **134** 555–64

[5] Tsui Y and Lu S 2008 Evaluation of the performance of a valveless micropump by CFD and lumped-system analyses *Sensors Actuators* **148** 138–48

[6] Cui Q, Liu C and Zha X F 2008 Simulation and optimization of a piezoelectric micropump for medical applications *Int. J. Adv. Manuf. Technol.* **36** 516–24

[7] Lee B and Kim E S 2000 Analysis of partly-corrugated rectangular diaphragms using the Rayleigh–Ritz method *J. Microelectromech. Syst.* **9** 399–406

[8] Olsson A, Stemme G and Stemme E 2000 Numerical and experimental studies of flat-walled diffuser elements for valve-less micropumps *Sensors Actuators* **84** 165–75

[9] Français O 2000 Analysis of an electrostatic microactuator with the help of matlab/simulink: transient and frequency characteristics *Proc. MSM 2000 (March)* pp 281–4

[10] ANSYS Incorporation home page http://www.ansys.com/ (visited on 08/07/2009)

[11] Jones I *et al* 2008 Wireless RF communication in biomedical applications *Smart Mater. Struct.* **17** 015050

[12] Hamsch M 2004 An interrogation unit for passive wireless SAW sensors based on Fourier transform *IEEE Trans. Ultrason. Ferroelectr. Freq. Control* **51** 1449–55

[13] Rangan C S, Sarma G R and Mani V S V 1983 *Instrumentation Devices and Systems* (New Delhi: Tata McGraw-Hill)

[14] Soin N and Majlis B Y 2006 Development of perfect silicon corrugated diaphragm using anisotropic etching *Microelectron. Eng.* **83** 1438–41

[15] Ke F, Miao J and Wang Z 2009 A wafer-scale encapsulated RF MEMS switch with a stress-reduced corrugated diaphragm *Sensors Actuators* A **151** 237–43

[16] Wang W J, Lin R M, Ren Y and Li X X 2003 Performance of a novel non-planar diaphragm for high-sensitivity structures *Microelectron. J.* **34** 791–6

[17] Giovanni M D 1982 *Flat and Corrugated Diaphragm Design Handbook* 2nd edn (New York: Dekker)

[18] Wang Y-G, Shi J-L and Wang X-Z 2009 Large amplitude vibration of heated corrugated circular plates with shallow sinusoidal corrugations *Appl. Math. Modelling* **33** 3523–32

[19] Dissanayake D W, Al-Sarawi S and Abbott D 2007 Surface acoustic wave device based electrostatic actuator for microfluidic applications *2nd Int. Conf. on Sensing Technology (Nov.)* pp 381–6

[20] Dissanayake D W, Al-Sarawi S F and Abbott D 2008 Electrostatic micro actuator design using surface acoustic wave devices *Smart Sensors and Sensing Technology* (*Lecture Notes in Electrical Engineering* vol 20) (Berlin: Springer) pp 139–51

[21] Gilbert J R, Ananthasuresh G K and Senturia S D 1996 3D modeling of contact problems and hysteresis in coupled electro-mechanics *Micro Electro Mechanical Systems* pp 127–32

[22] Hu Y C, Chang C M and Huang S C 2004 Some design considerations on the electrostatically actuated microstructures *Sensors Actuators* A **112** 155–61

[23] Bao M-H 2000 Basic mechanics of beams and diaphragm structures *Micro Mechanical Transducers: Pressure Sensors, Accelerometers, and Gyroscopes* (*Hand Book of Sensors and Actuators* vol 8) (New York: Elsevier) pp 23–87

[24] Füldner M, Dehé A and Lerch R 2005 Analytical analysis and finite element simulation of advanced membranes for silicon microphones *IEEE Sensors J.* **5** 857–63

[25] Nisar A, Afzulpurkar N, Mahaisavariya B and Tuantranont A 2008 Multifield analysis of a piezoelectrically actuated valveless micropump *Sensors Transducers J.* **94** 176–95

[26] Lakshminarayana H 2004 *Finite Elements Analysis: Procedures in Engineering* (Hyderabad, India: Universities Press)

[27] HD MicroSystems, Parlin, NJ 2008 *PI-2600 LX Series, Low Stress Polyimides, Product Information and Process Guidelines* April 2008

[28] Kazaryan A A 2000 Thin-film capacitive pressure transducers which operate during the deformation of products *Meas. Tech.* **43** 38–43

[29] Gad-el-Hak M 2002 *The MEMS Handbook* (New York: CRC Press)

[30] MEMS and Nanotechnology Clearinghouse. Material http://www.memsnet.org/material/ (visited on 08/07/2008)

[31] Rousche P J, Pellinen D S, Pivin D P Jr, Williams J C, Vetter R J and Kipke D R 2001 Flexible polyimide-based intracortical electrode arrays with bioactive capability *IEEE Trans. Biomed. Eng.* **48** 361–71

[32] Dissanayake D W, Al-Sarawi S, Lu T-F and Abbott D 2008 Design and characterisation of micro-diaphragm for low power drug delivery applications *Active and Passive Smart Structures and Integrated Systems*; *Proc. SPIE* **6928** 69282P

[33] Lee S and Kim K J 2006 Design of IPMC actuator-driven valve-less micropump and its flow rate estimation at low Reynolds numbers *Smart Mater. Struct.* **15** 1103–9

[34] Olsson A 1998 Valve-less diffuser micropumps *PhD Thesis* Instrumentation Laboratory, Department of Signals, Sensors and Systems, Royal Institute of Technology, Sweden

[35] Woias P 2001 Micropumps: summarizing the first two decades *Microfluidics and BioMEMS*; *Proc. SPIE* **7268** 39–52